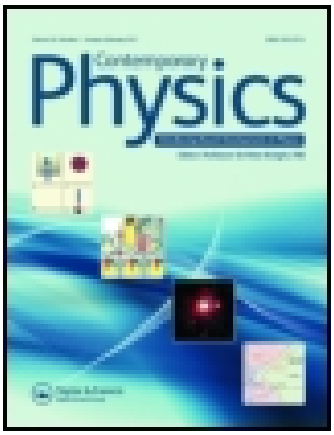

Contemporary Physics

Publication details, including instructions for authors and subscription information:
http://www.tandfonline.com/loi/tcph20

Computerized scatter correction in diagnostic radiology

K. P. Maher & J. F. Malone

Published online: 08 Nov 2010.

To cite this article: K. P. Maher & J. F. Malone (1997) Computerized scatter correction in diagnostic radiology, Contemporary Physics, 38:2, 131-148, DOI: 10.1080/001075197182469

To link to this article: http://dx.doi.org/10.1080/001075197182469

Contemporary Physics, 1997, volume 38, number 2, pages 131 – 148

Computerized scatter correction in diagnostic radiology

K. P. MAHER† and J. F. MALONE‡

The field of diagnostic radiology continues to generate interesting lines of physics research even though it is over a century since X-rays were first used for medical imaging. One of these concerns scatter processes which are well known to be a major influence on the quality of X-ray images. The components, effects, reduction and measurement of scatter and the potential of computerized scatter correction schemes are reviewed in this paper. The effect of scatter on indices of image quality is considered using analytical models and published experimental results. Scatter measurement based on the widely applied opaque disc technique and a novel aperture technique are discussed in detail. In addition, computerized scatter correction based on convolution filtering schemes and interpolated local sampling schemes are critically reviewed. The treatment focuses on fluoroscopy – fluorography, although extensive reference is also made to other radiographic imaging techniques.

1. Introduction

It is about 100 years since radiographs were first produced for medical diagnostic purposes (Rosenow 1995). From a medical perspective, the radiograph provides information on a broad range of disease conditions and radiography has therefore been widely applied in medicine (Grainger and Allison 1992). The conventional approach involves a projection imaging technique (figure 1) where a broad radiation beam from an X-ray tube (XRT) irradiates the patient and the projected image is recorded by an image receptor. Figure 2 shows illustrative examples of such X-ray images. Complementary medical information can be obtained using other imaging techniques, such as computerized axial tomography scanning, nuclear medicine, ultrasound and magnetic resonance imaging. However, these newer techniques represent only about 25% of medical imaging examinations and projection radiography continues to be widely applied (for example, AIHW (1994)).

From a physical perspective, the X-ray image represents a two-dimensional recording of radiation intensities emerging from the irradiated object. The physical parameters which characterize a radiograph therefore relate to the ability to resolve points in two-dimensional space and to discriminate X-ray intensity at these locations. A radiograph is also characterized by stochastic effects resulting from the random nature of X-ray production and absorption. In addition, the cost of acquiring diagnostic information using radiography is the radiation dose to the patient, and a substantial reduction in dose has been achieved through developments in image receptor technology (for example, Marshall *et al.* (1994)).

The production of scattered radiation within the irradiated object has a major influence on the detectability of details within images, and conventional mechanisms for handling its effects are directed at reducing the intensity of this radiation reaching the image receptor (Sorenson and Niklason 1988). Such reduction techniques can be applied, in many instances, only at the expense of a threefold or greater increase in dose. Scattering events within the image receptor also have an influence on detectability, depending on the type of technology used. The typical technology is based on fluorescent screen – photographic film receptors, and efforts to reduce scattering effects have concentrated on minimization of X-ray and light scattering. The technology applied for the production of sequences of radiographic images, that is for *fluoroscopy* and *fluorography*, is based on photoelectronic devices, and efforts to reduce scattering effects have concentrated on minimization of X-ray, light and electron scattering. Such efforts have had limited success, however, and significant scatter signals are generated with current fluoroscopy systems (Luhta and Rowlands 1990). It is apparent that conventional methods of scatter reduction are unlikely to influence the scatter introduced by such image receptors directly, and efforts have therefore been directed at compensation for scatter effects *post*-image acquisition (Seibert *et al.* 1985). These compensation techniques can also be applied to image signals arising from scattering events within the patient

†*Author's address:* Department of Medical Radiations Science, Royal Melbourne Institute of Technology, Australia.

‡*Author's address:* Department of Medical Physics and Bioengineering, St James's Hospital, Dublin and Trinity College Dublin, Ireland.

0010-7514/97 $12.00

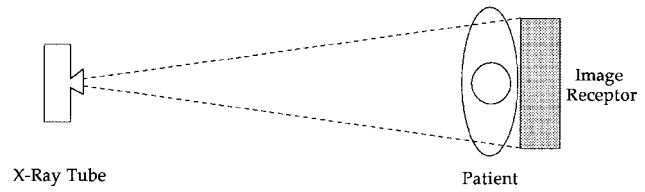

Figure 1. Illustration of broad-beam projection radiography.

(Love and Kruger 1987). As a consequence, they may obviate the need for conventional scatter reduction methods and may provide possibilities for reductions in patient radiation dose.

Scatter compensation has been facilitated by the use of computerized image processors interfaced to the image receptor to form a *digital fluoroscopy–fluorography* system (Maher and Malone 1986). Compensation techniques which have been developed typically involve computation of a scatter field and subtraction of this field from the conventional image (Love and Kruger 1987). These techniques are also applicable to other radiographic imaging methods which involve computer processing, such as photostimulable phosphor imaging (Floyd *et al*. 1992a).

This paper reviews the components (section 2), effects (section 3), reduction (section 4), measurement (section 5) and the potential for computerized correction (section 6) of scatter. The treatment focuses on fluoroscopy–fluorography, although extensive reference is also made to other radiographic imaging techniques. In addition to the references cited in this paper the reader is referred to textbooks such as those by Barrett and Swindell (1981), Macovski (1983), Webb (1988) and Hasegawa (1991) for treatment of basic aspects of radiographic physics and instrumentation.

2. Components of scatter

Conventional radiography involves a broad-beam projection imaging technique (figure 1). Tungsten anode XRTs, with potentials of 25–150 kV and focal spot sizes of 0·5–1 mm, are typically used. The beam size is adjusted, using rectangular collimators at the output of the XRT, to define an area of up to about 35 cm by 45 cm at the image receptor, depending on the examination. A photographic film–intensifying screen system is the image receptor typically used for the production of single radiographic images, although recent innovations include photostimulate phosphor (Floyd *et al*. 1991) and amorphous selenium (Neitzel *et al*. 1994) systems. The image receptor for fluoroscopy typically consists of an X-ray image intensifier optically coupled to a video camera (Maher and Malone 1986). The components of scatter in broad beam projection radiography result from the generation of off-focus radiation (OFR) in the XRT, scattered radiation within the patient and veiling glare within the image receptor (Plenkovich 1989).

OFR results from X-ray emission from points other than the focal spot of the X-ray tube and is thought to arise from emissions generated throughout the anode material by recoil electrons. OFR generally adds a spatially uniform background signal to the image. It should also be noted that emissions from secondary microfocal spots have recently been discovered, which may add a high spatial frequency structure to this uniform background (Roeck *et al*. 1992). Estimates of the magnitude of OFR indicate that it is quite sensitive to collimation of the X-ray tube and may range from 2·5% to 8% of the focal radiation exposure (Birch 1976).

The Compton effect and coherent scattering are the major scattering processes within the patient in the range of X-ray energies used for most medical diagnostic purposes. The situation for tissue is illustrated in figure 3 (ICRU 1992). It can be seen that the mass attenuation coefficient resulting from the photoelectric effect decreases rapidly with increasing energy, as does the attenuation coefficient for coherent scattering, with that for the Compton effect remaining relatively constant (about 0·16 to about 0·2 $cm^2\ g^{-1}$) over the energy range. In addition, it can be seen that the Compton effect becomes the dominant process above about 30 keV. It can therefore be inferred that this scattering process should provide a large contribution to X-ray attenuation in most diagnostic examinations. In the case of chest radiography, for example, the intensity of scattered radiation has been found to dominate the primary radiation intensity for all anatomical locations (Sorenson and Niklason 1988).

Scattering processes within the imaging receptor are collectively referred to as veiling glare. The X-ray image intensifier (XII) has been widely assumed to be the dominant source of such scatter in fluoroscopy (Luhta and Rowlands 1990), and it has been estimated that this contribution represents about 25% of the image signal (Seibert *et al*. 1985). In addition, the influence of the coupling optics has been shown to contribute about 20% of the veiling glare signal from the combined XII and coupling optics (Bromberg and Bickford 1984). Furthermore, Bitler *et al*. (1992) have shown that the video camera contributes a small but significant veiling glare signal. Thus it seems reasonable to expect that veiling glare within the whole imaging chain is an important contributor to the scatter signal in fluoroscopic imaging.

DC voltages on the video signal generated by the fluoroscopy system have also been shown to reduce image contrast (Maher *et al*. 1987), with the effect being equivalent to that of a spatially uniform scatter signal. It is apparent, however, that this contribution may be eliminated, ideally, through appropriate adjustment of the electronic circuitry of the imaging system.

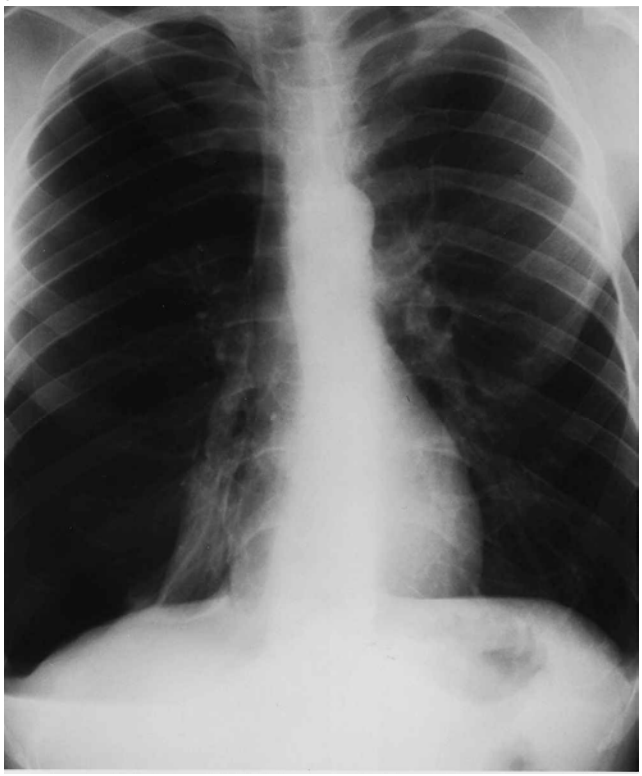

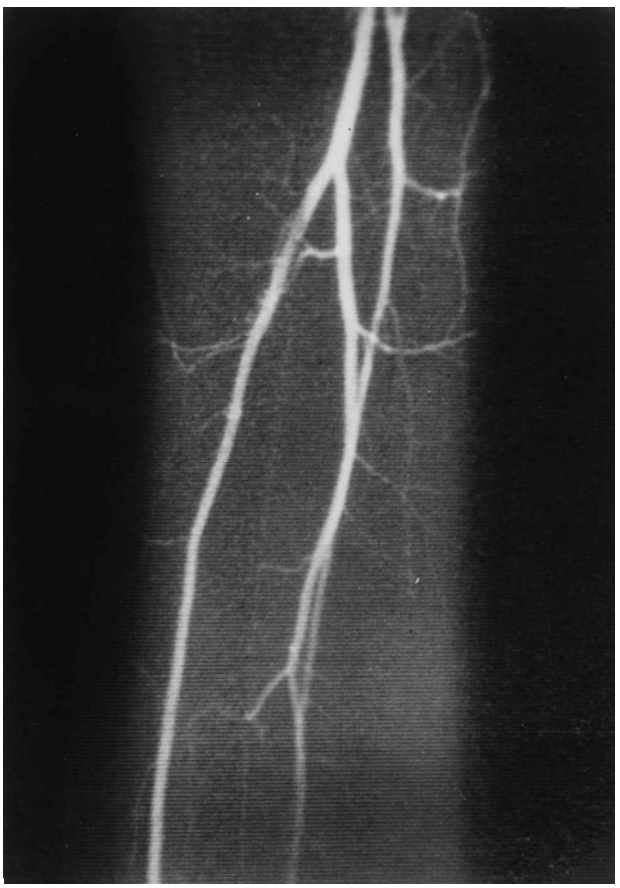

Figure 2. Illustrative examples of projection radiographs. (*a*) Chest radiography is frequently used to provide information regarding the respiratory system, the heart and bones of the thorax. Mammography (*b*) provides vital information regarding breast cancer. (*c*) Angiography provides detailed information regarding blood vessels; here a computerized subtraction technique is used to remove tissue and bone image data in order to highlight a radio-opaque dye injected into the blood-stream to portray, in this case, arteries in the leg.

3. Effects of scatter

Scatter results in contrast reduction, densiometric inaccuracy and loss of image sharpness. These effects are individually considered below, firstly using a simple model of broad area contrast loss (section 3.1) and then by a consideration of the effects of scatter on image sharpness (section 3.2). Scatter also increases image noise (Macovski 1983). However, this feature is neglected in the treatment below and noiseless imaging is assumed to allow attention to focus on the general arguments.

3.1. *Contrast loss*

Consider a typical radiographic imaging task of detecting an object contained within a material of different attenuation properties; a good example is the detection of bone within tissue as shown in figure 4. This example is chosen purely for illustrative purposes, and it should be appreciated that the general argument may be applied to any radiographic detection task. Assume that in figure 4 monoenergetic radiation is used, and that, initially, no scattered radiation is generated. Defining the contrast between the transmitted intensities as

$$C = \ln I_1 - \ln I_2, \tag{1}$$

it is possible to show that

$$C = (\mu_b - \mu)t_b, \tag{2}$$

where μ_b is the linear attenuation coefficient of bone, μ is the linear attenuation coefficient of tissue and t_b is the bone thickness. Equation (2) indicates that the contrast is directly proportional to bone thickness, with a constant of proportionality equal to the difference in the photoelectric attenuation coefficients of bone and tissue. It is apparent that contrast increases linearly with increasing bone thickness in this ideal situation, which suggests that estimates of bone thickness could be obtained directly from a contrast measurement.

It should be noted that hardening of a polychromatic beam is neglected in the simple treatment here, so as not to complicate the argument with a feature which has been demonstrated to be relatively unimportant in comparison with the effects of scatter (Harrison 1985).

In the presence of scattered radiation, the transmitted intensities, assuming a simple additive process, are increased by the detected scatter intensity, so that the contrast is now given by

$$C = \ln \frac{1 + \mathrm{SPR}}{\exp -(\mu_b - \mu)t_b + \mathrm{SPR}}, \tag{3}$$

where SPR is the ratio of the intensity of scattered radiation to that of primary radiation.

Contrast, calculated using equation (3), is plotted against bone thickness in figure 5(*a*) for various values of the SPR. It is seen that, when the SPR = 0, the condition specified in equation (2) is obtained and that, when the SPR increases, the relationship between contrast and bone thickness decreases in slope. In other words, the bone detection task becomes more difficult, as the intensity of scattered radiation, relative to the primary radiation, increases. In addition, it is seen in figure 5(*a*) that the slope of each individual relationship, when the SPR is greater than zero, decreases with increasing bone thickness. It is apparent that a reduced ability to discriminate bone thickness results, leading to a loss in the quantitative fidelity of a contrast measurement.

Figure 5(*a*) also indicates that a relatively small amount of scattered radiation results in a significant loss of contrast. Figure 5(*b*) illustrates this point from a different perspective, where it is seen that bone contrast decreases rapidly as the SPR increases. It can be seen that the contrast of a 1 cm bone thickness, for example, is reduced to 50% of the no-scatter level when the SPR is just 0·6.

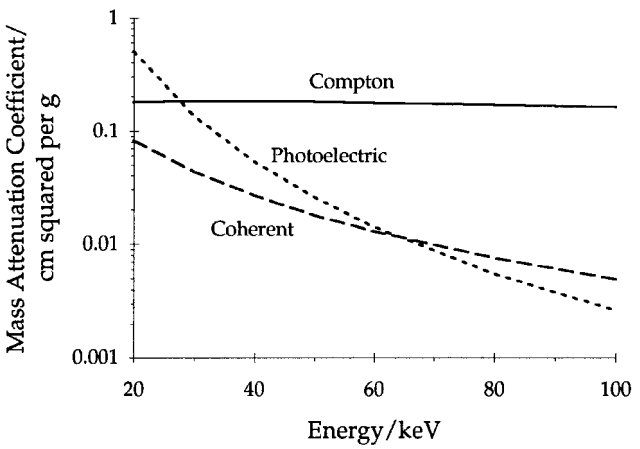

Figure 3. Energy dependence of the mass attenuation coefficients for soft tissue.

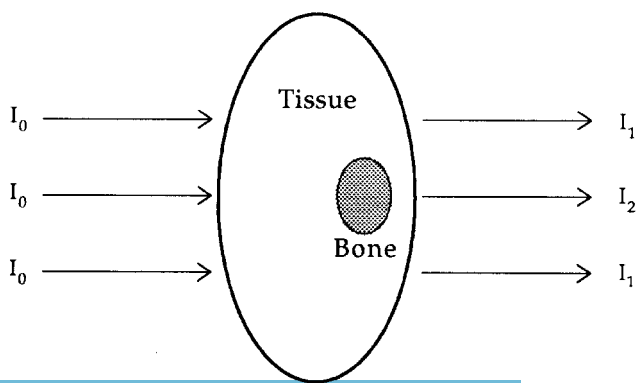

Figure 4. Illustration of a section of bone within tissue irradiated with an incident beam of intensity I_0 to give transmitted intensities of I_1 and I_2.

The magnitude of the SPR can be estimated using a broad-beam analytical model (Macovski 1983), which involves considering a parallel radiation beam striking a cylindrical phantom and circular image receptor (figure 6). Consider an incremental layer of thickness dz within the scattering medium at a distance Z from the exit surface. The detected scattered radiation signal results from contributions which include

(1) the radiation intensity incident on the layer, that is $I_0\exp[-\mu_t(L-Z)]$, where μ_t is the total attenuation coefficient for the scattering material,
(2) the probability of scattering within the layer, which is dependent on the scattering attenuation coefficient, μ_{sr},
(3) the fraction β of scattered photons which are scattered forwards and
(4) the scattered radiation collection solid angle Ω at the detector plane.

Assuming that the collection solid angle is constant for each point in the detector plane and that the contribution of multiple scattering is given by a multiplicative factor $2\mu_{sr}L$ (Macovski 1983), the SPR is given by

$$\mathrm{SPR} = 2\mu_{sr}^2\beta L\left[L + R - (L^2 + R^2)^{1/2}\right]\left(1 - \frac{s}{(R^2 + s^2)^{1/2}}\right), \quad (4)$$

which indicates that the SPR is dominated by factors associated with the imaging geometry.

Equation (4) is in a convenient form for exploring the dependence of the SPR on geometrical factors encountered in clinical imaging conditions. The dependence of SPR on the thickness of scattering material is shown in figure 7, the 20 cm beam radius data representing imaging conditions used, for example, in chest radiography. It is seen that the SPR rises rapidly with increasing thickness, reflecting the increasing number of scattering sites within the scattering material, with the scattered radiation intensity equalling the primary intensity at a thickness of about 5 cm for a beam radius of 20 cm, and becoming about ten times the primary intensity at 20 cm thickness, and about 18 times the primary intensity at 30 cm thickness. It is apparent that equation (4) indicates that scattered radiation is likely to represent a major component of the image signal in clinical imaging situations.

This expectation has been confirmed by experimental measurement. For example, measurements from a chest phantom at 120 kV_p using a $CaWO_4$ screen (Sorenson and Niklason 1988) found that the SPR ranged from a value of about 1·2 in the lung fields, to about 10 in the central mediastinum. In addition, measurements from 102 chest radiographs obtained at 95 kV_p using a photostimulable phosphor imaging system (Floyd *et al.* 1992b) found that the average value of the SPR ranged from about 2 in the lung fields, to 19 in the middle of the mediastinum. It is apparent from these reported measurements, and from figure 5, that scattered radiation is likely to have a considerable effect on the contrast of features in clinical images.

The SPR includes the contribution from veiling glare in fluoroscopic–fluorographic imaging. A veiling glare fraction of about 25% has been measured for fluoroscopy–fluorography systems, on the basis of an analytical model of light diffusion in the output phosphor of the image intensifier (section 3.2). It seems reasonable to expect that the contrast loss in fluoroscopic–fluorographic imaging is even greater than that expected on the basis of the above discussion.

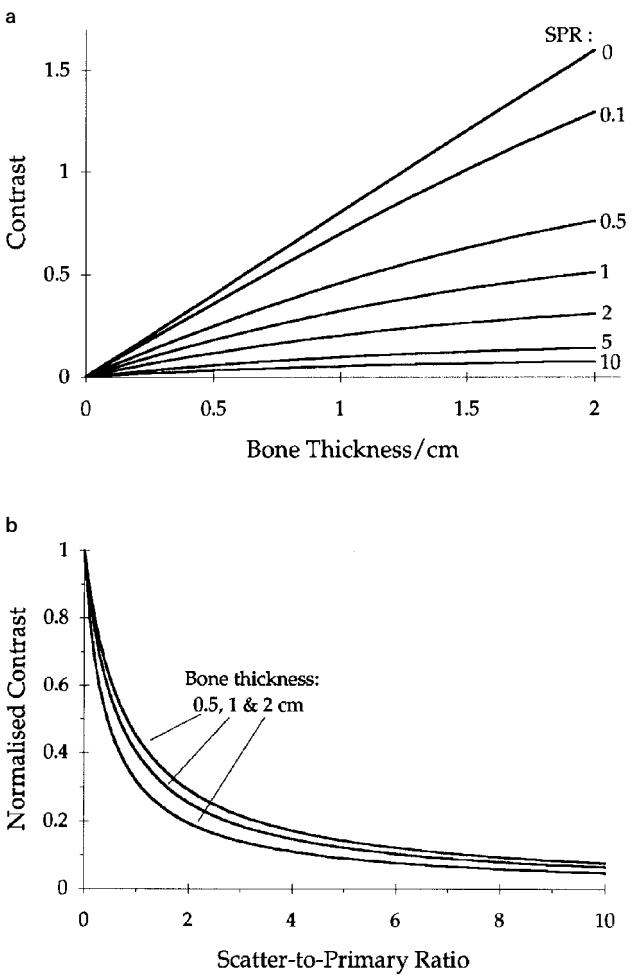

Figure 5. (*a*) **Contrast against bone thickness, calculated using equation (3), assuming that $\mu_b = 1{\cdot}276\ cm^{-1}$ and $\mu = 0{\cdot}261\ cm^{-1}$ at 40 keV (ICRU 1992), for various values of the SPR. (*b*) Contrast, normalized to unity, of 0·5, 1 and 2 cm thicknesses of bone, against the SPR calculated using equation (3).**

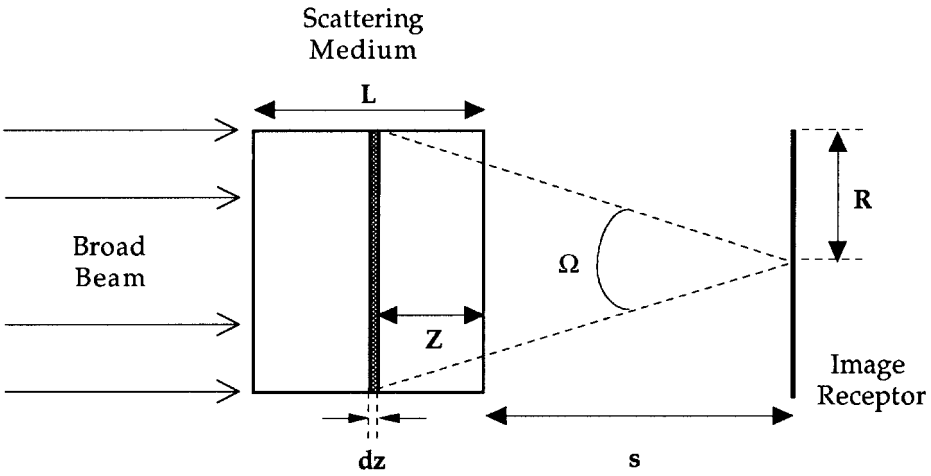

Figure 6. Illustration of a cylinder of homogeneous scattering material of thickness L at a distance s from the image receptor, irradiated with a broad radiation beam.

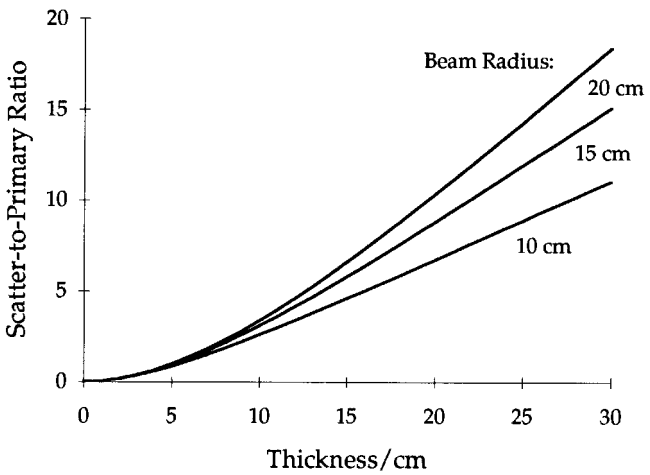

Figure 7. Dependence of the SPR on phantom thickness, for beam radii of 10, 15 and 20 cm and no air gap, calculated using equation (4), assuming that $\beta = 0.55$ and $\mu_{sr} = 0.2\ cm^{-1}$.

3.2. *Loss of sharpness*

In addition to contrast loss, the other effect of scatter, of relevance to this paper, is a reduction in image sharpness. It is apparent that the diffuse nature of X-ray scattering within the patient, and of scattering events within the image receptor, is likely to result in a blurring of image details. A mathematical expression for such blurring is developed and conceptual approaches to its characterization are considered below. Noiseless imaging conditions and energy-independent detection are assumed, and spatial information is neglected, in the treatment, as was the case in section 3.1

Consider the process of imaging a homogeneous scattering material. The radiation intensity distribution transmitted through the material can be expressed as

$$I_t = I_p + I_{sr}, \tag{5}$$

where I_p represents the primary radiation intensity distribution and I_{sr} represents the scattered radiation intensity distribution. The scattered radiation distribution can be considered (Love and Kruger 1987) to be equivalent to a diffused version of the primary distribution, so that

$$I_{sr} = \mathrm{SPR}\ I_p ** h_{sr}, \tag{6}$$

where ** denotes a two-dimensional convolution and h_{sr} represents the point spread function (PSF) of scattered radiation, that is the blurring of image data due to scatter processes.

The form of the scattered radiation PSF can be determined using both analytical modelling and Monte Carlo simulation techniques. Analytical modelling based on a single-scatter approximation (Barrett and Swindell 1981) indicates that scattered radiation gives rise to broad structureless skirts around the image of a pencil X-ray beam, for example with the radial spread of the scattered radiation PSF extending beyond 50 cm, for a 10 cm thickness of scattering material and a 10 cm air gap. In addition, such modelling suggests that the scattered radiation PSF becomes broader with increasing absorber thickness and increasing air gap. Furthermore, it implies that, although the skirts have a very low amplitude, their contribution very quickly becomes significant when the contributions from many such pencil beams are superimposed to form a broad radiation beam.

Monte Carlo techniques have been widely used for the analysis of photon transport problems (Morin 1988). The basic approach involves the random selection of where and how photons interact within an absorber, as well as the variables which govern the outcomes of each interaction.

These variables are derived from the theoretical behaviour of each interaction process, supported by data from experimentally derived tables of interaction cross-sections (for example Hubbell *et al.* (1975)). It is apparent that the approach lends itself to the study of scattered radiation in diagnostic radiography since the overall imaging process can be viewed as a cascade of stochastic processes, from radiation production through interaction with the patient to image transduction. In addition to consideration of the various interaction mechanisms, Monte Carlo simulation also requires consideration of the geometric relationship between the source, the scattering material and the image receptor. Such simulation has indicated that multiple scattering becomes highly probable at large absorber thicknesses as well as at higher X-ray energies, with photons undergoing more than ten scattering events not being uncommon (Chan and Doi 1988). It can therefore be inferred that an analytical approach based on the single-scatter approximation alone is unlikely to provide an adequate description of the situation, and that inclusion of a multiple-scattering term in, for example, the broad-beam analytical model discussed earlier (equation (4)) is justified.

The PSF of scattered radiation can be computed using Monte Carlo simulation by considering the response of the scattering material to a pencil X-ray beam. Such an approach has generated PSFs which are of very long range (Boone and Seibert 1988), extending to about 10 cm radial distance for a scattering material 10 cm thick without any air gap, and to beyond 20 cm for a 20 cm thickness of scattering material with a 4 cm air gap, and which, in general, are of broadly similar appearance to those obtained using analytical modelling.

It is apparent from the above that both analytical modelling and Monte Carlo simulation indicate that the scattered radiation PSF is broad for homogeneous scattering materials. The situation is illustrated in figure 8, where the PSF is derived on the basis of a radially symmetric distribution (Wagner *et al.* 1988b)

$$h_{sr}(r) = \frac{s^3}{(r^2 + s^2)^{1/3}}, \tag{7}$$

where r is the radial distance and s is the air gap.

It can therefore be inferred that scattered radiation is a low-spatial-frequency phenomenon, which should give rise to a blurring of image details and a low-frequency drop (LFD) in the modulation transfer function (MTF). This inference is supported by experimental evidence which indicates that scattered radiation decreases the limiting resolution, decreases modulation at all spatial frequencies and increases the magnitude of the LFD (Fenster *et al.* 1986). It is apparent that the LFD dependence indicates that the contrast of broad objects should be sensitive to the intensity of scattered radiation, which is consistent with the prediction of the simple model of contrast loss presented earlier (equation (3)).

When the transmitted radiation distribution is detected by the image receptor, it can be considered that a portion of the energy is mapped directly, with the remainder undergoing further diffusion (Seibert *et al.* 1985). Thus the detected signal distribution, assuming an additive process and 100% detection efficiency, can be expressed as

$$I_d = (1 - \rho) I_t + \rho I_t * * h_{vg}, \tag{8}$$

where ρ is the veiling glare fraction and h_{vg} is the veiling glare PSF. Thus, from equations (5) and (6), the detected intensity distribution is given by

$$I_d = (1 - \rho)(I_p + \text{SPR}\ I_p * * h_{sr}) + \rho(I_p + \text{SPR}\ I_p * * h_{sr}) * * h_{vg}. \tag{9}$$

This equation indicates that the detected distribution consists of the directly mapped primary and scattered radiation distributions, summed with a diffused version of this transmitted distribution.

The PSF of veiling glare has been studied using an energy diffusion model for light diffusion in the output phosphor of an image intensifier (Seibert *et al.* 1985). This model assumes that the output phosphor is the main source of energy diffusion, to generate the following expression:

$$h_{vg}(r) = \frac{\rho \exp(-r/k)}{2kr}, \tag{10}$$

where r is the radial distance and k expresses the width of a symmetrical distribution of diffused energy. The variables ρ and k can be determined from a plot of the logarithm of the contrast ratio against the radius of opaque discs (Seibert *et al.* 1984). On this basis, k has been determined at 3–12·5 cm, depending on the image intensifier (Seibert *et al.* 1984, Faulkner *et al.* 1989).

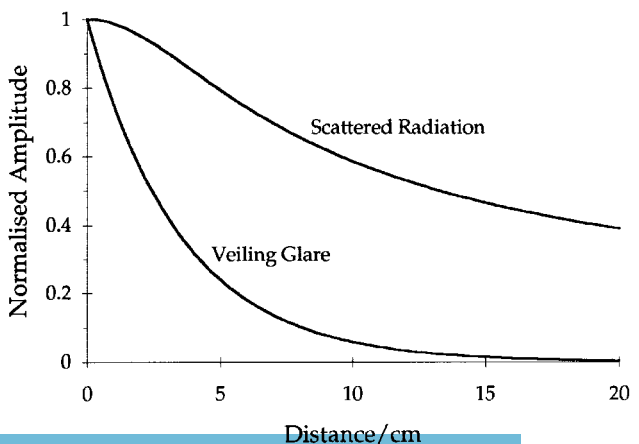

Figure 8. The PSF of scattered radiation calculated using equation (7) for a 5 cm air gap, and the form of the veiling glare PSF (for k= 3·5 cm) using the exponential term in equation (10).

A criticism of this approach is the assumption that veiling glare results from the output phosphor only. It should be noted that Seibert *et al.* (1984) indicate that it is possible to derive this assumption from information presented by Vosburgh *et al.* (1977). It is important to note, however, that measurements for just one image intensifier are quoted by Vosburgh *et al.* (1977) the results being summarised in table 1. It is seen in the table that the output phosphor (and window) is the major source of veiling glare for the image intensifier in question, contributing about 55% of the total veiling glare. However, it can also be seen that the input stages also contribute significantly (about 35%), in line with conclusions by Heidsieck (1989) of 35–40%, and by Luhta and Rowlands (1990) of about 50%.

Neglecting this criticism, the exponential term in equation (10) is nevertheless plotted in figure 8 for $k = 3{\cdot}5$ cm (Seibert *et al.* 1984) to illustrate that this model suggests that the veiling glare PSF is likely to be narrower than the scattered radiation PSF. It can therefore be inferred that veiling glare should cause blurring of image details, but not to the extent caused by scattered radiation.

4. Conventional methods of scatter reduction

It is apparent from equation (3) that contrast should increase when the magnitude of the SPR is reduced. Conventional methods of scatter reduction achieve this prior to image reception and include the use of grids, air gaps and beam collimation. These methods reduce the scattered radiation component of the overall scatter signal at the image receptor, do not completely eliminate it and do not influence the veiling glare component directly. In addition, the use of grids and air gaps result in substantial increases in radiation dose (Sorensen and Niklason 1988). The discussion below focuses on the contrast improvement provided by these methods and neglects, for clarity of presentation, any energy-dependent characteristics of the image receptor.

Table 1. Contributions of various stages to the measured reciprocal contrast ratios for a pre-1973 X-ray image intensifier. (Adapted from Vosburgh *et al.* (1977).)

Source of veiling glare	Percentage of total
Input phosphor	7·6
Phosphor curvature	19·9
X-ray scattering by front window	8·1
Light reflections by tube interior	7·8
Output phosphor and window	56·7

4.1. *Scatter reduction grids*

Grids were originally introduced over 70 years ago. They consist typically of a series of lead strips separated by an interspace material, of lower atomic number, and are placed in close contact with the face of the image receptor (Sorenson and Niklason 1988). An example is a grid with lead strips of thickness 0·05 mm and an interspace thickness of 0·3 mm so that a pitch of about 30 strips cm^{-1} is obtained. The strips can be parallel, crossed or angled towards the focal spot, so that most of the primary radiation passes unimpeded to reach the image receptor, and most of the scattered radiation is absorbed by the strips. The resultant effect therefore is a reduction in the SPR.

Grids are characterized by a number of features which include the grid ratio, that is the height of the lead strips: the interspace width ratio, and typical values range from 4:1 to 16:1. The effect on the SPR in chest radiography is illustrated by the data in table 2. It can be seen that both the 6:1 and the 12:1 grids provide substantial reductions in the SPR. However, it is apparent from figure 5 that, while each grid should provide an improvement in contrast, neither is likely to restore the scatter-free condition completely. Nevertheless grids are widely applied in diagnostic radiography as a result of ease of application in clinical situations and the improvements in image quality obtained.

Table 2. Scatter-to-primary ratios for various regions of a chest phantom obtained using two different grids, two different air gaps and a slit imaging technique. (Adapted from Niklason *et al.* (1981).)

	SPR			
Technique	Lung	Rib	Heart	Mediastinum
No grid, 3 cm air gap	1·22	1·78	4·26	10·1
6:1 grid, 3 cm air gap	0·59	0·75	1·7	3·55
12:1 grid, 3 cm air gap	0·35	0·47	0·85	1·33
No grid, 30 cm air gap	0·54	0·61	1·78	4·56
Slit imaging, 6:1 grid, 15 cm air gap	0·27	0·3	0·52	0·67

4.2. *Air gaps*

Air gaps between the patient and the image receptor reduce the SPR by decreasing the solid angle presented by the receptor to the scattering sites. The effect of an air gap is illustrated in figure 9, where equation (4) has been evaluated for different thicknesses of homogeneous scattering material and a beam radius of 20 cm, that is conditions which approximate to chest radiography. It can be seen that the SPR decreases rapidly with increasing air gap, reducing by 50% with an air gap of about 12 cm, in the case of a 20 cm thickness of scattering material, and to 10% with an air gap of about 27 cm. This theoretically derived dependence is supported by published experimental data (table 2). It can be seen in the table that a substantial reduction in SPR is obtained with a 30 cm air gap, and that the reduction is similar to that provided by a 6:1 grid. However, it is apparent from figure 5 that, while an air gap should generate substantial improvements in contrast, it is unlikely to restore the scatter-free condition completely. In addition, it should be noted that this approach to scatter reduction results in magnified images, with increased focal spot blurring. This latter feature can be reduced, however, by using relatively large focal spot-to-image distances, but at the expense of increased XRT loading.

4.3. *Beam collimation*

Collimation of the X-ray beam reduces the SPR by decreasing the number of scattering sites within the patient. This point is illustrated in figure 10, where equation (4) is evaluated for different thicknesses of scattering material. It can be seen that the SPR decreases rapidly as the beam size is reduced, by 50% in the case of the 20 cm thickness when the radius is reduced from 20 to about 7 cm, and to 20% at a radius of about 3 cm. This feature has led to the development of imaging systems which are based on assembling many small-field images of the patient to form a composite image. These systems use single- or multiple-scanning fanbeams, and numerous designs have been developed (Plenkovich 1989), a good example of which is the widely reviewed AMBER system which incorporates a scanning slit beam with a mechanism for local exposure control (Noordveld *et al.* 1989). The performance of these systems is illustrated by the case of a slit imaging device in table 2, where it is seen that considerably greater reductions in SPR are obtained relative to the use of a 30 cm air gap, or to the use of grids alone. However, it is again apparent that the scatter-free condition (figure 5) is unlikely to be completely restored. In addition, it should be noted that these systems typically involve the use of cumbersome mechanical apparatus (for collimating and scanning the X-ray beam), require significantly longer exposure times than conventional broad-beam imaging systems and generate considerable loading of the XRT (Sorenson and Niklason 1988). As a result, they have not found wide clinical application.

5. Measurement of scatter

Numerous investigations have been undertaken to measure scatter intensities in radiographic imaging. Table 3 provides a list of illustrative examples of these investigations. An approach common to many of these investigations involves measuring the signal detected in the shadow of an opaque disc. This approach is considered in section 5.1 and is followed by consideration of an alternative technique based

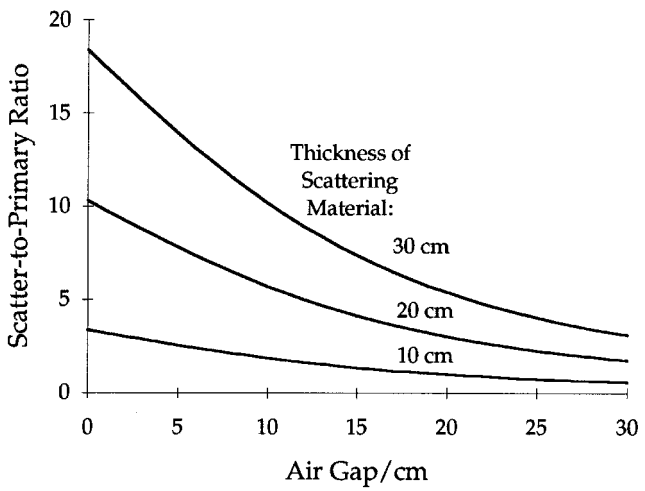

Figure 9. Dependence of the SPR on air gap, for 10, 20 and 30 cm thicknesses of scattering material and a 20 cm beam radius, calculated using equation (4), assuming that $\beta = 0{\cdot}55$ and $\mu_{sr} = 0{\cdot}2\ cm^{-1}$.

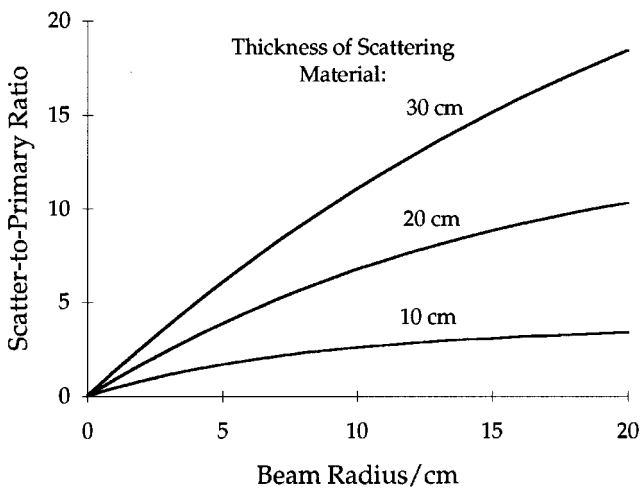

Figure 10. Dependence of the SPR on beam radius, for 10, 20 and 30 cm thicknesses of scattering material and no air gap, calculated using equation (4), assuming that $\beta = 0{\cdot}55$ and $\mu_{sr} = 0{\cdot}2\ cm^{-1}$.

Table 3. Examples of investigations which have been undertaken to measure scatter intensities in radiographic imaging.

Subject	Reference
Influence of patient thickness, field size and air gap	Burgess and Pate (1981)
Chest radiography	Floyd *et al.* (1992b)
Mammography	Barnes and Brezovich (1978)
Scanning slit imaging	Doi *et al.* (1986)
Equalization radiography	Noordveld *et al.* (1989)
Duel energy imaging	Shaw (1992)
Electronic collimation	Plenkovich (1989)
Computed radiography	Floyd *et al.* (1991)
Large-field image intensifiers	Fujita *et al.* (1987)
Solid-state X-ray imaging detectors	Sones *et al.* (1990)
Verification of Monte Carlo simulations	Chan and Doi (1983)
Computerized scatter correction schemes	Love and Kruger (1987)
Tissue density measurement	Cockin *et al.* (1985)
Densitometry in digital subtraction angiography	Maher *et al.* (1987)
Spectral content of scatter	Kubota *et al.* (1994)
Intensity of coherent scatter	Johns and Yaffe (1983)

on the use of an aperture (section 5.2). This latter technique is considered from the perspective of the broad beam analytical model which was discussed earlier (section 3.1). In addition, other, less widely reported methods are described in section 5.3.

5.1. *Opaque disc technique*

The opaque disc technique is based on using a small lead disc, placed on the XRT side of the scattering medium, to absorb totally the radiation incident on the disc. As a result, any signal detected in the shadow of the disc results from scatter processes only. It is apparent that this technique can underestimate the true scatter signal, however, since the disc blocks the incident radiation from a volume of scattering material which would normally generate scattered radiation. It is also apparent that this unirradiated volume is related to the size of the disc used. It is possible to account for this underestimation by plotting the signal measured in the disc's shadow (or either the derived scatter fraction or SPR) for a range of disc sizes, and extrapolating to zero disc size. As a result, a measure of scatter is obtained which is representative of that present in the absence of the disc.

It has been noted that variation exists in the form of data extrapolation which has been employed in the literature (Maher 1993) with some investigators using linear extrapolation with disc area as the independent variable and others using linear extrapolation with disc diameter as the independent variable, or nonlinear extrapolation with either disc area or disc diameter as the independent variable. The linear relationship with area is based on considering the area of a disc to be directly proportional to the volume of the column of primary radiation which is blocked by that disc (Chan and Doi 1983). No explicit justification can be found readily in the literature for the other forms of data extrapolation, although it can be inferred that a quadratic fit to diameter data is consistent with the reasoning of Chan and Doi (1983). The opaque disc technique has been compared with the aperture technique of scatter measurement (section 5.2) in an attempt to identify the appropriate form of extrapolation in fluoroscopy (Maher 1993). It was found that linear extrapolation of diameter data gave a SPR estimate which was within 1% of that provided by the aperture technique. In addition, it was found that the relationship with disc area was nonlinear so that linear extrapolation substantially underestimated the SPR. It is therefore apparent that linear extrapolation of disc diameter data is appropriate in fluoroscopy and that large underestimates of the SPR can result when linear extrapolation of area data is unwittingly applied.

Finally, an extension to the opaque disc technique has been reported recently in relation to measurement of scatter intensities in clinical images (Floyd *et al.* 1992a). The extension involves using two image receptors, separated by about 1 cm, with a lead disc sandwiched between them, and lends itself to photostimulable phosphor imaging. The conventional imaging plate is used to record the usual radiograph and the second plate records a scatter signal for the region behind the lead disc. An empirical relationship was established between the recorded scatter fraction and that obtained using the standard lead disc technique and was used to translate the 'posterior' disc measurements. The technique is useful for determining scatter fractions in

clinical images because data can be acquired without subjecting the patient to a second exposure, and without recording disc shadows on the conventional image which might obscure anatomical details of interest.

5.2. *Aperture technique*

The principle that a narrow radiation beam can be used to minimize the detection of scattered radiation is appreciated widely in the field of radiation detection (Johns and Cunningham 1983). When a narrow-beam measurement is assumed to represent the intensity of primary radiation, it is apparent that the scatter intensity may be obtained by subtraction from a broad-beam measurement.

Gould and Hale (1974) used this approach to investigate the effect of air gaps in chest radiography. The detector consisted of a calcium tungstate intensifying screen coupled to a photomultiplier tube (PMT), and a narrow-beam condition was obtained using 'a very narrow beam' and a second collimator which was (apparently) placed between the screen and the PMT. No details of the size of the narrow beam were reported, however, and replication of the exact experimental technique is therefore not possible.

A reasonable question to ask about this technique relates to the accuracy of the primary signal obtained using a narrow aperture, in that a small scatter component could conceivably exist. An estimate of the magnitude of the scatter signal with small apertures can be obtained using the broad beam analytical model which was described in section 3.1. Figure 11 shows the SPR dependence on aperture size up to a radius of 0·15 cm for scattering media of thicknesses 15, 20 and 25 cm. It can be seen that the SPR increases with increasing beam radius. It can also be seen that the SPR is less than about $0{\cdot}5 \times 10^{-3}$ for a beam of radius 0·1 cm for the three thicknesses of scattering media,

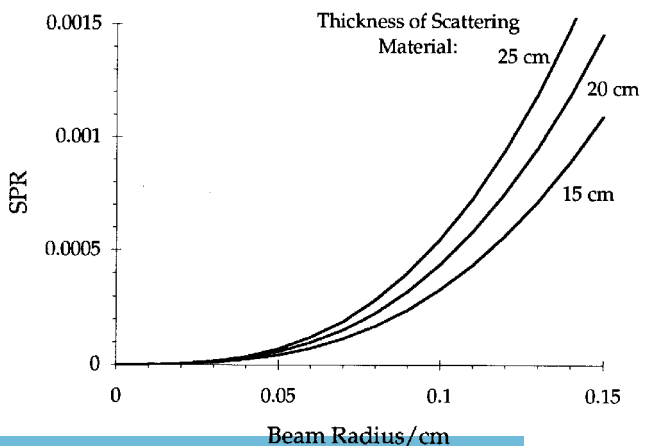

Figure 11. The dependence of SPR on the radius of a narrow X-ray beam for 15, 20 and 25 cm thicknesses of scattering material and an air gap of 1 cm, calculated using equation (4).

which implies that the scatter component is minute relative to the primary component, and which also implies that the total transmitted signal contains information predominantly from the primary component.

It may be difficult in practice to detect such a minute scatter signal. For example, with an 8-bit digital fluoroscopy system, the quantization step size is about 4×10^{-3} units and it is unlikely that a scatter component which is less than the step size can be readily detected. Thus it can be inferred, assuming that equation (4) represents a reasonable description of the imaging situation, that an aperture of radius 0·1 cm is unlikely to generate a detectable scatter signal with an 8-bit imaging system, and that the aperture signal therefore represents in essence a scatter-free signal. In addition, it is apparent that a quantization level of more than 10 bits would be required to detect this scatter signal, assuming noiseless imaging.

Evidence that a narrow radiation beam provides a negligible scatter signal has been obtained experimentally in digital fluoroscopy (Maher 1993) on the basis of obtaining an aperture signal which was independent of air gap. A 2·5 mm aperture, which was placed 40 cm from the focal spot of the XRT, was used. It is apparent that this technique could represent a simple, accurate method of scatter measurement, which does not require extrapolation from a series of measurements, as with the opaque disc technique (section 5.1), and which may lend itself to clinical studies in that the narrow-beam exposure required may not add in any significant way to the patient dose received from the conventional radiograph.

5.3. *Other techniques of scatter measurement*

Other techniques which have been developed to measure scatter include the use of a slit profile, opaque bars, translucent discs, aperture – disc assemblies and the LFD of the modulation transfer function. These techniques are briefly described below for completeness.

5.3.1. *Slit profile technique.* This technique has been applied to scatter measurement in fan-beam imaging (Plenkovich 1989). It involves placing a lead blocker within the fore-slit of the fan-beam assembly, with the blocker size equal to the slit width. Line profiles are obtained for two adjacent parallel lines lying perpendicular to the slit direction: one line through the disc, and the other through a section of the slit not covered by the disc. The SPR can be estimated by determining the primary component and the scatter component by integrating under the line profiles between boundaries defined by the full width at half-maximum of the net primary peak.

5.3.2. *Opaque bar technique.* Lead bars, placed between the XRT and the scattering material, have been used to

evaluate the accuracy of computerized scatter correction schemes (Love and Kruger 1987, Floyd *et al.* 1989) (see section 6.2). Here the computed scatter signal for a line profile across an image is compared with the signal detected in the shadow of an opaque bar placed along the same line. From the earlier discussion (section 5.1), it is apparent that this approach is likely to underestimate the true scatter signal by a factor which is dependent on the unirradiated volume of scattering material.

5.3.3. *Translucent disc technique.* Since the standard opaque disc technique can obscure a region of a clinical image, Cocklin *et al.* (1985) used a translucent disc in patient studies. The transparent disc should be sufficiently translucent to allow some clinical information to be recorded in its shadow. This technique is based on knowledge of the exact attenuation properties of the disc material and the assumption that the scatter signal in the disc region is the same as that for the region surrounding the disc. The true scatter signal is obtained by relating the shadow signal to that of the surrounding region. It is apparent from the earlier discussion (section 5.1) that, once again, a disc size dependence may also require consideration when this technique is employed.

5.3.4. *Primary modulation–demodulation technique.* A novel approach has recently been proposed which is based on using a translucent sheet with an aperture on the XRT side of the scattering material, and a disc of the same translucency as the sheet, and of an equivalent size as the aperture, on the detector side of the scattering material (Shaw 1992). The aperture and disc should be along the same line of sight, so that the aperture modulates the distribution of primary radiation and the disc subsequently demodulates it. As a result, the attenuation of primary radiation should be unaffected, while the scattered radiation generated within the patient will be attenuated by the disc. The scatter signal can then be obtained by relating the signal for the region of the aperture–disc to that of the surrounding region. An advantage of this approach is that it allows the SPR to be determined from a single image, whereas two images are required when the standard opaque disc technique is used.

5.3.5. *Low-frequency drop technique.* The LFD of the MTF has been used to investigate the effect of beam width on scatter intensities generated in fan-beam imaging (Cunningham *et al.* 1987). The MTF is determined from a line profile perpendicular to a lead edge, by differentiating it prior to Fourier transformation. It is apparent that, while this approach is not directly dependent on any shadowing-type effect, it is nevertheless cumbersome to employ because of the complexity of the mathematical computations involved and requires knowledge of the sampling aperture of the imaging system in order to avoid undersampling of the data (Fujita *et al.* 1992).

6. Computerized methods of scatter correction

Computerized methods of correcting for scatter effects in radiographic images involve the use of computer imaging processing to compensate for scatter signals following image reception. An additive model for the compounded signals from primary radiation and scatter processes is generally assumed, so that the correction process involves determination of the spatial distribution of scatter signals, followed by subtraction of this scatter distribution from the detected image (Love and Kruger 1987). It is possible to consider that such scatter correction schemes are equivalent to a form of background subtraction. It is apparent, however, that the spatial distribution of such background signals is unlikely to be uniform, so that digital background suppression using, for example the 'windowing' function available on digital fluoroscopy systems, does not provide the necessary spatial sensitivity (Maher and Greaves 1992).

Two major approaches to computerized scatter correction have been developed. One approach specifically addresses the loss of both contrast and sharpness due to scatter (Love and Kruger 1987), and methods based on this approach are referred to here as convolution filtering schemes (section 6.1). The second approach specifically addresses the loss of contrast (Wagner *et al.* 1988a), and methods based on this approach are referred to here as scatter sampling schemes (section 6.2). Other, less widely reported approaches to computerized scatter correction are described briefly in section 6.3.

6.1. *Convolution filtering schemes*

Convolution filtering schemes are based on the assumption that the distribution of scatter signals in an image is equivalent to a blurred version of the distribution of primary signals (Love and Kruger 1987). The rationale for these schemes is outlined below, the approach drawing on the mathematical treatment which was used to describe sharpness loss in section 3.2. Spatial information is neglected, once again, for clarity. In addition, noiseless imaging is assumed in order that attention may focus on the general argument, although such an assumption is hardly valid in real imaging situations (Cohen *et al.* 1982), and although it can be demonstrated that noise is the sole obstacle to perfect restoration of the desired information (Frieden 1979).

Consider that the detected signal intensity distribution in an image is given by

$$I_d = I_p + I_s \tag{11}$$

where I_p is the primary signal intensity distribution and I_s is the scatter signal intensity distribution. This scatter

distribution can be considered to be equivalent to a blurring of the primary distribution (Love and Kruger 1987), so that

$$I_s = \text{SPR}\ I_p ** h_s, \tag{12}$$

where SPR is the ratio of the scatter signal to the primary signal, h_s is the scatter PSF and ** denotes a two-dimensional convolution. The primary distribution is therefore given by

$$I_p = I_d - \text{SPR}\ I_p ** h_s, \tag{13}$$

The image restoration problem, on the surface, becomes one of estimating h_s, and solving equation (13) to restore the primary distribution. However, it should be noted that the unknown I_p is also present on the right-hand side of the equation. This limitation has been approached in the literature by using the detected distribution as an estimate of the primary distribution (Love and Kruger 1987, Molloi and Mistretta 1988), so that equation (13) becomes

$$I_d = I_d - W(I_d ** h_s), \tag{14}$$

where W is the ratio of the scatter signal to the total signal, that is the scatter fraction, and $(I_d ** h_s)$ represents a low-pass filtered version of the detected image.

The filtering scheme may be implemented in either the spatial domain (Love and Kruger 1987) or the spatial frequency domain (Seibert and Boone 1988). The spatial domain approach, expressed by equation (14), involves applying digital kernels to blur the detected image, weighting the blurred image, and subtracting the result from the detected image. The frequency domain approach involves generating the frequency spectrum of the detected image by using a Fourier transformation, dividing the spectrum by a filter function (determined from the scatter PSF) and generating the inverse Fourier transform of the filtered spectrum (Floyd *et al.* 1989). Filtering schemes which have been developed can be categorized as analytical and empirical approaches and are considered in turn below.

The analytical approach is based on deconvolving the detected image using filters which are determined from analytical models of the scatter PSF (Seibert and Boone 1988). The approach has been implemented with digitized film–screen images using a spatially invariant exponential PSF (Floyd *et al.* 1989), and overestimates of the scatter signal were obtained. The approach has also been applied to fluoroscopic images, following an initial correction for veiling glare, using a spatially invariant Gaussian PSF (Seibert and Boone 1988), and residual scatter signals were obtained. The initial veiling glare correction is based on a similar approach where images of an unattenuated radiation field are deconvolved using an analytical expression for the veiling glare PSF, for example equation (10).

The empirical approach is based on generating a blurred version of the detected image using blurring functions which are determined empirically through minimization of the error between estimated and measured scatter levels in images of anthropomorphic phantoms (Love and Kruger 1987). Results of such error assessment have shown that a spatially variable weighting factor (i.e. W in equation (14)) provides improvements over a spatially invariant weighting factor (Molloi and Mistretta 1988), and that exponential blurring kernels with a full width at half maximum as large as 75 × 75 pixels (Love and Kruger 1987), and spatially variable kernel sizes (Kruger *et al.* 1994) are required. Errors have been determined typically by comparing scatter levels measured using the opaque bar technique (section 5.3.2) with those computed by blurring functions, and rms errors as low as 4–8% have been obtained (Love and Kruger 1987).

Evaluation of the performance of convolution filtering schemes has indicated substantial improvements in contrast (Seibert and Boone 1988). However, it can be noted from the referenced literature that evaluations of improvements in image sharpness have not been made explicitly, except in the case of Faulkner *et al.* (1989) where an improvement in the edge response function of veiling glare corrected images was obtained. Finally, it can be inferred that sophisticated computing resources, by today's clinical standards, are required in order to implement convolution filtering schemes at reasonable speeds because of the necessity to generate very large blurring kernels (Kruger *et al.* 1994), or to implement Fourier filtering on large two-dimensional arrays of data (Seibert and Boone 1988).

6.2. *Scatter sampling schemes*

Scatter sampling schemes involve determination of the scatter signal in individual pixels of an image in order to determine the distribution of scatter signals. Methods of determining the scatter signals in individual pixels include the generation of fan beams of scattered radiation by scanning opaque bars during the exposure (Shaw and Plewes 1985, Wagner *et al.* 1988a), the isolation of scatter signals through comparison of images acquired at different air gaps (Boone 1986), and on interpolation between local scatter measurements obtained using an array of opaque discs (Wagner *et al.* 1988a, Maher and Greaves 1992, Lo *et al.* 1994). The scanning bars method involves the use of specialized mechanical scanning apparatus, and extended exposure times. In addition, the air gap comparison method requires correction for image magnification effects. Interpolated local sampling schemes, however, are attractive in terms of their relative simplicity and are considered in more detail below.

A basic assumption of interplated local sampling schemes is that the scatter distribution is equivalent to a low frequency surface (Wagner *et al.* 1988a). This surface can be determined from equation (9) to be given by

$$I_s = (1-\rho)(SPR\ I_p ** h_{sr}) + \rho(I_p + SPR\ I_p ** h_{sr}) ** h_{vg}. \quad (15)$$

The proposition that the scattered radiation distribution ($SPR I_p ** h_{sr}$), is equivalent to a smooth surface has been provided by Wagner *et al.* (1988a), where a typical —6 dB cut-off frequency of the scattered radiation transfer function is estimated, using the Fourier transform of equation (7), to be in the range from 1 cycle/15 cm to 1 cycle/50 cm for air gaps from 3 to 10 cm respectively, that is spatial periods which are of the same magnitude as typical radiographic field sizes. It can be inferred from section 3.2 that the veiling glare transfer function has a higher cut-off frequency. Its —6 dB point can be estimated from the Fourier transform of the veiling glare PSF (equation (10)) in the work of Seibert *et al.* (1985) and its measured widths (Seibert *et al.* 1984, Faulkner *et al.* 1989), to be in the range from 1 cycle/1·5 cm to 1 cycle/6 cm. It is therefore apparent that equation (15) indicates that the scatter distribution in an image may be considered to be equivalent to a smooth surface, arising from a low-frequency scattered radiation distribution which is modulated by the higher-frequency content of the veiling glare distribution.

The question then, for interpolated local sampling schemes, is how to sample this surface adequately. A critical sampling distance (Bracewell 1965) of 0·75 – 3 cm is indicated on the basis of the above estimates of the cut-off frequencies for the veiling glare transfer function. It can therefore be inferred that local measurement of scatter intensities in, for instance, a square array of points, with a spacing of at least the critical sampling distance, should provide adequate sampling of the scatter distribution. Local scatter measurement has been obtained using an array of lead discs (Wagner *et al.* 1988a, Maher and Greaves 1992, Lo *et al.* 1994).

The computation of surfaces has been studied extensively in the field of computer-aided graphic design (Dahmen *et al.* 1990). Methods which have been used with interpolated local sampling schemes include the use of two-dimensional least-squares fitting (Love *et al.* 1986, Wagner *et al.* 1988a), filtration with sinc and jinc functions (Wagner *et al.* 1989), two-dimensional polynomial interpolation (Maher and

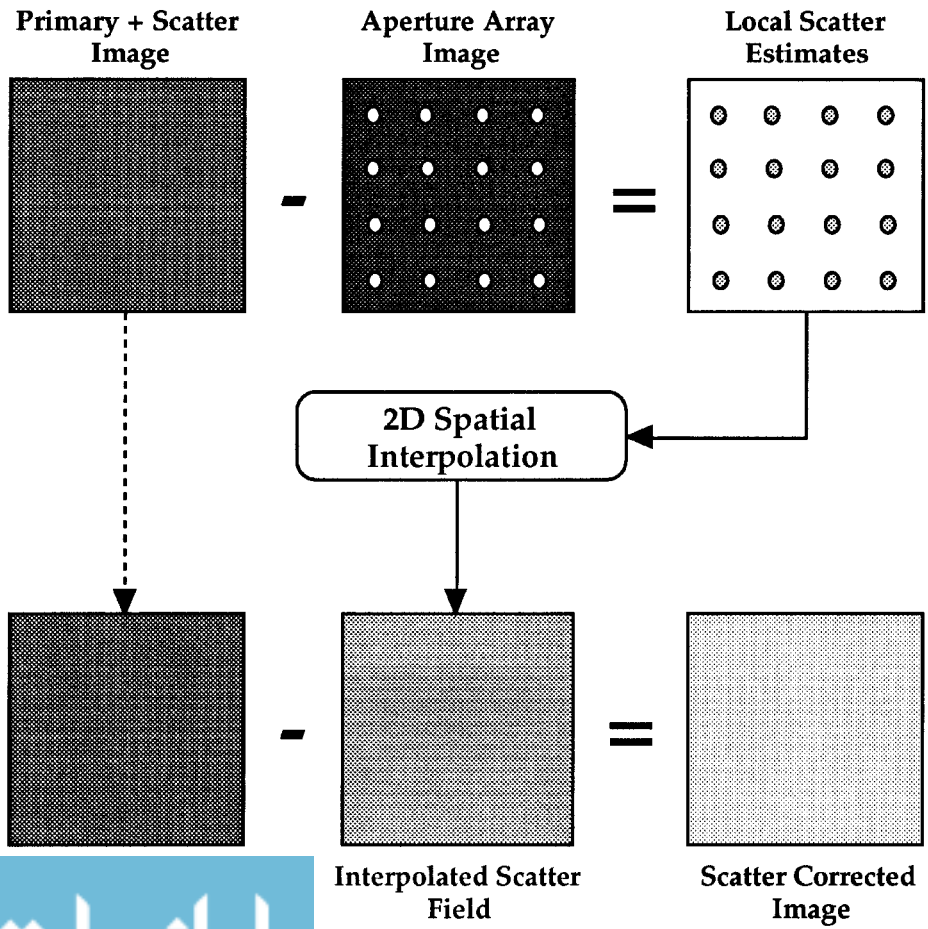

Figure 12. Schema for an interpolated aperture array scheme for scatter correction: 2D, two-dimensional.

Greaves 1992) and two-dimensional bicubic spline interpolation (Lo *et al.* 1994). Least-squares fitting has been found to generate errors of about 15% at the points of measurement (Love *et al.* 1986), and interpolated filtration has been found to generate unacceptable aliasing artefacts (Wagner *et al.* 1989). Polynomial interpolation, on the other hand, uses polynomials whose order is one less than the number of sampling points in one dimension of the array and is attractive because of its ability to return interpolated values which are equal to the actual values at the points of measurement (Press *et al.* 1986). However, this form of interpolation is limited to arrays of no greater than about 5 ×5 sampling points, because of the tendency for instabilities to be introduced when higher-order terms are included in the polynomials. Bicubic spline interpolation also has the ability to return interpolated values which are equal to the actual values at the points of measurement and can be used with larger arrays of sampling points (Lo *et al.* 1994).

Evaluation of the performance of interpolated local sampling schemes has demonstrated substantial improvements in contrast (Wagner *et al.* 1988a), in spatial uniformity (Wagner *et al.* 1988a, Maher and Greaves 1992), in subjectively assessed contrast-detail performance (Maher and Greaves 1992), and in the visualization of structrues in high-scatter regions of chest radiographs (Baker *et al.* 1993).

A disadvantage of interpolated local sampling schemes is the requirement for two exposures of the patient: one without, and the other with an array of opaque discs in place. It is apparent that the approach could be extended to the use of arrays based on the posterior opaque disc (section 5.1) and the primary modulation – demodulation (section 5.3.4) techniques of scatter measurement, so as to eliminate the need for a second radiation exposure. However, the posterior opaque disc technique does not lend itself to fluoroscopic imaging, by its nature, although the primary modulation – demodulation technique might be applicable. Another possibility for reducing patient exposure with interpolated local sampling schemes is to extend the aperture technique of scatter measurement (section 5.2) to two dimensions, that is to use an array of apertures to provide the local scatter measurements. A possible scheme, illustrated in figure 12, involves generating an array of local primary measurements using an aperture array, substracting these data from the unprocessed image to generate an array of local scatter measurements, and then interpolating the scatter measurements to form the scatter field, which can be subtracted from the unprocessed image to generate a scatter-corrected image. It is apparent that the exposure increase with this scheme is dependent on the relative magnitudes of the area of the broad beam used for the uncorrected (i.e. the primary plus scatter) image and the integrated area of the narrow beams generated by the aperture array. Another possible advantage of this approach over schemes based on arrays of opaque discs

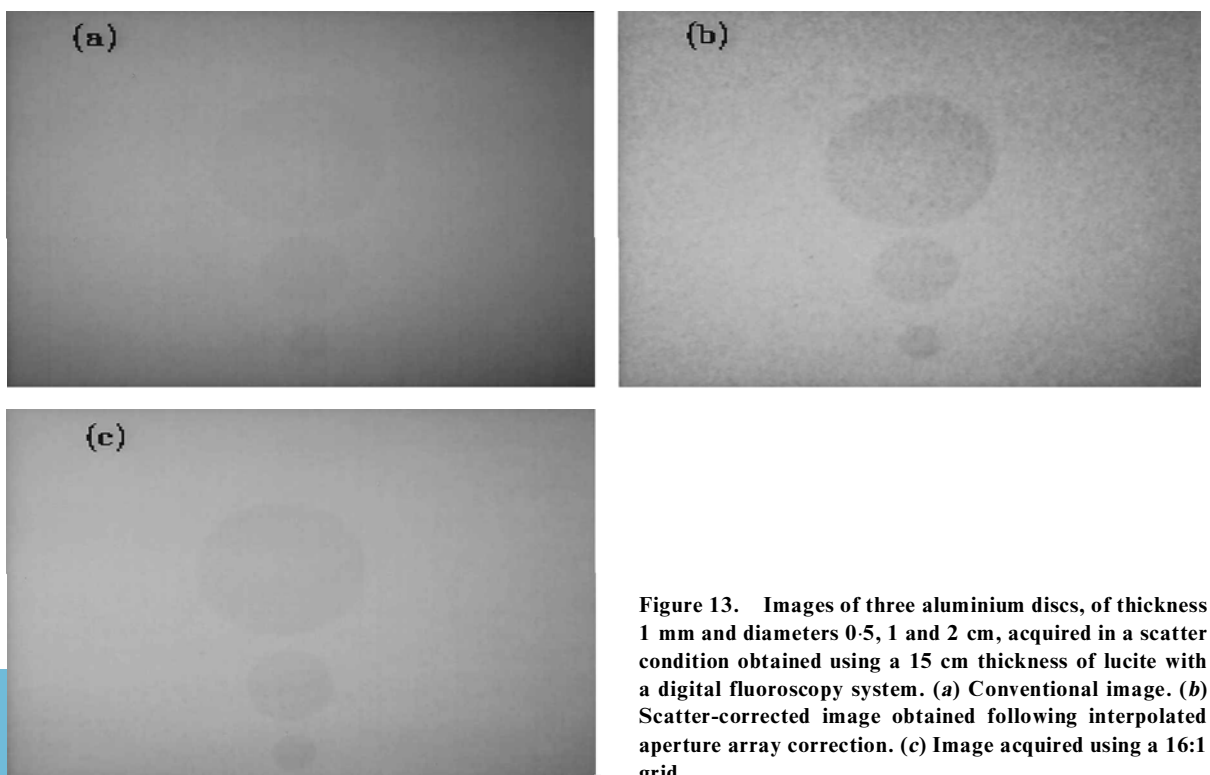

Figure 13. Images of three aluminium discs, of thickness 1 mm and diameters 0·5, 1 and 2 cm, acquired in a scatter condition obtained using a 15 cm thickness of lucite with a digital fluoroscopy system. (*a*) Conventional image. (*b*) Scatter-corrected image obtained following interpolated aperture array correction. (*c*) Image acquired using a 16:1 grid.

is a more accurate method of determining scatter signals, in that it was noted earlier that scatter measurement using a lead disc requires correction for the effect of the unirradiated volume of scattering material (section 5.1), while the aperture technique may provide a scatter-free signal directly (section 5.2).

The potential of this approach is illustrated in figure 13. The images are of three aluminium discs, of thickness 1 mm and diameters 0·5, 1 and 2 cm, which were acquired in a scatter condition obtained using a 15 cm thickness of lucite scattering material with a digital fluoroscopy system. This imaging condition was chosen to simulate the detection of subtle features in routine radiography and a homogeneous background was chosen to optimise the signal detection task. Scatter correction was achieved using a 4×4 array of 1·5 mm apertures and two-dimensional third-order polynomial interpolation (figure 12). A distinct improvement in the visibility of the discs is apparent in the scatter-corrected image (figure 13(*b*)), where the contrast (equation (1)) of the discs is improved relative to the uncorrected image (figure 13(*a*)) by a factor of about 2·8. Figure 13(*c*) results when a 16:1 grid is used in the image acquisition process to simulate a powerful conventional method of scatter reduction (section 4) and has been included for comparison purposes. An improvement in contrast relative to the uncorrected image is also apparent in figure 13(*c*). However, the improvement in this case is a factor of about 1·7, that is roughly 40% lower than that for computerized scatter correction. It should be noted that an eightfold increase in radiation exposure is typical when such a grid is used (Sorenson and Niklason 1988), and that the exposure increase with the scatter correction scheme is a negligible 1·5%. Computerized scatter correction would therefore appear to have potential for clinical application.

An increase in mottle, however, can be seen in figure 13(*b*) in addition to the contrast improvement. This effect is directly related to the removal from the raw image data of a noise-free scatter field (as is generated in the two-dimensional interpolation process) and it can be concluded on this basis that the reduction in signal-to-noise ratio (SNR) is given by the reciprocal of the primary fraction. It is therefore apparent that scatter corrected images should contain a noise-print reflecting the distribution of primary radiation signals. It is also apparent that this feature is characteristic of any correction scheme which involves the subtraction of a smooth background image, be it based on scatter sampling, convolution filtering or other correction method. However, it can be shown analytically that the improvement in broad-area contrast more than offsets the SNR reduction for typical radiographic detection tasks. It is therefore apparent that scatter correction should generate an outcome of potential benefit to the detection of features in radiographic images.

6.3. *Other computerized methods of scatter correction*

A number of other scatter correction schemes have been reported in the literature. These are briefly described below for completeness.

White *et al.* (1985) reported on a method, based once again on acquiring two images, with the scatter intensity varied using a grid for one of the images. A processing algorithm was devised on the basis of considering the primary and scatter transmissions of the grid, so as to permit a scatter distribution to be isolated from the two acquired images. No improvement in structural detail of radiographs of a chest phantom was observed with the method, a finding which was attributed to the assumption used in the processing algorithm of spatially invariant primary and scatter transmissions for the grid.

Fahimi and Macovski (1989) describe an iterative technique which utilizes scatter signals behind the collimators of a 'coned-down' X-ray image, and assumptions which include a scatter distribution which contains low-frequency components only. An improvement in image contrast for a chest phantom was obtained.

Floyd *et al.* (1993) reported the development of an iterative maximum-likelihood expectation maximization algorithm for chest radiography, in which scatter is modelled by a spatially invariant exponential PSF, and image noise is assumed to be Poisson distributed. Substantial improvements in contrast, in SNR and in the visualization of structures within a chest phantom were obtained. This approach has recently been extended using a Bayesian image processing algorithm (Floyd *et al.* 1994).

Finally, Fivez *et al.* (1995) describe a convolution filtering scheme which uses an array of transparent shields to estimate local scatter signals (section 5.3.3). The scheme requires only one exposure of the patient and therefore has potential for clinical application.

7. Conclusion

Medical imaging today consists of a broad range of imaging modalities which, in addition to projection radiography, includes computer tomography, magnetic resonance imaging, nuclear medicine imaging and ultrasonography. The recently introduced modalities are critically dependent on computer processing for image production and computers have also found application in the archival and rapid transmission of medical images. Scatter correction is an application of computer processing to conventional radiography. The approach is not unique to radiography however and has also been applied in X-ray computed tomography, emission computed tomography and positron emission tomography. This reflects the generalized nature of the approach and indicates how an understanding of the basic physics of the imaging process can be used to design computer processing methods.

It can be noted from section 6 that reasonably crude indicators have been used to express the performance of scatter correction schemes. These indicators have included error estimation for both primary and scatter signals, as well as measures of broad area contrast, and have typically excluded resolution and noise properties. It is apparent that the reduction in SNR is likely to be a major disadvantage of correction schemes which involve subtraction of a smooth scatter field. Nevertheless, improvements in the visibility of low contrast discs can be seen in figure 13, which suggests that low contrast details in clinical images should be more conspicuous following scatter correction. Future work in this area could therefore be directed at semisubjective end points, such as contrast-detail analysis, to determine the extent to which the SNR reduction relative to the improvement in broad area contrast affects the imaging performance of computerized scatter correction, relative both to uncorrected images and to images acquired using conventional scatter reduction methods. The potential of computerized noise reduction of scatter-corrected images also warrants investigation from this perspective. In addition, consideration of clinical trials of the approach could extend from analysis of images of anthropomorphic phantoms with simulated lesions so that the combined effect of contrast improvement and SNR reduction on diagnostic accuracy can be gauged.

Acknowledgement

This work was partially supported by contract No. F13P-CT920014 of the European Community's Radiation Protection Programme.

References

AIHW, 1994, *Health Technology Statistics Bulletin*, No. 4 (Canberra: Australian Institute of Health and Welfare).

Baker, J. A., Floyd, C. E., Lo, J. Y., and Ravin, C. E., 1993, *Invest. Radiol.*, **28,** 667.

Barnes, G. T., and Brezovich, I. A., 1978, *Radiology*, **126,** 243.

Barrett, H. H., and Swindell, W., 1981, *Radiological Imaging: The Theory of Image Formation, Detection and Processing*, Vols 1 and 2 (New York: Academic Press), pp. 631–635.

Birch, R., 1976, *Br. J. Radiol.*, **49,** 951.

Bitler, W., Coffin, J., Doesschate, W., Langdon, R., and Murphy, G., 1992, *Medical Imaging VI: Instrumentation*, Proceedings of the SPIE, Vol. 1651 (Bellingham, Washington: SPIE), p. 263.

Boone, J. M., 1986, *Med. Phys.*, **13,** 319.

Boone, J. M., and Seibert, J. A., 1988, *Med. Phys.*, **15,** 713.

Bracewell, R. N., 1965, *The Fourier Transform and Its Applications* (New York: McGraw-Hill), pp. 189–194.

Bromberg, N., and Bickford, J., 1984, *Application of Optical Instrumentation in Medicine XII*, Proceedings of the SPIE, Vol. 454 (Bellingham, Washington: SPIE), p. 387.

Burgess, A. E., and Pate, G., 1981, *Med. Phys.*, **8,** 33.

Chan, H.-P., and Doi, K., 1984, *Phys. Med. Biol.*, **28,** 109.

Chan, H.-P., and Doi, K., 1988, *Monte Carlo Simulation in the Radiological Sciences*, edited by R. L. Morin (Boca Raton, Florida: CRC Press), pp. 103–191.

Cocklin, M. L., Lams, P. M., and Schroter, R. C., 1985, *Application of Optical Instrumentation in Medicine XIII*, Proceedings of the SPIE, Vol. 553 (Bellingham, Washington: SPIE), p. 340.

Cohen, G., Wagner, K. K., and Rauschkolb, E. N., 1981, *Radiology*, **144,** 613.

Cunningham, I. A., Hobbs, B. B., Gerson, R. K., and Fenster, A., 1987, Medical Imaging, Proceedings of the SPIE, Vol. 767 (Bellingham, Washington: SPIE), p. 186.

Dahmen, W., Gasca, M., and Micchelli, C. A. (editors), 1990, *Computation of Curves and Surfaces* (Dordrecht: Kluwer).

Doi, K., Fujita, H., Ohara, K., Ono, K., Matsui, H., Giger, M. L., and Chan, H.-P., 1986, *Radiology*, **161,** 513.

Fahimi, H., and Macovski, A., 1989, *IEEE Trans. Med. Imag.*, **8,** 56.

Faulkner, K., Kotre, C. J., and Louka, M., 1989, *Proceedings of the Third International Conference on Image Processing and its Applications* (London: Institution of Electrical Engineers), pp. 669–673.

Fenster, A., Cunningham, I. A., and Hobbs, B. B., 1986, *Med. Instrum.*, **20,** 173.

Fivez, C., Wambacq, P., Vuylsteke, P., and Schoeters, E., 1995, *Pattern Recognition Image Anal.*, **5,** 107.

Floyd, C. E., Baker, J. A., Lo, J. Y., and Ravin, C. E., 1992a, *Invest. Radiol.*, **27,** 119.

Floyd, C. E., Baker, J. A., Lo, J. Y., and Ravin, C. E., 1992b, *Radiology*, **183,** 857.

Floyd, C. E., Baydush, A. H., Lo, J. Y., Bowsher, J. E., and Ravin, C. E., 1993, *Invest. Radiol.*, **28,** 427.

Floyd, C. E., Baydush, A. H., Lo, J. Y., Bowsher, J. E., and Ravin, C. E., 1994, *Invest. Radiol.*, **29,** 904.

Floyd, C. E., Beatty, P. T., and Ravin, C. E., 1989, *Invest. Radiol.*, **24,** 30.

Floyd, C. E., Lo, L. Y., Chotas, H. G., and Ravin, C. E., 1991, *Med. Phys.*, **18,** 408.

Frieden, B. R., 1979, *Picture Processing and Digital Filtering*, edited by T. S. Huang (New York: Springer), pp. 177–248.

Fujita, H., Doi, K., MacMahon, H., Kume, Y., Giger, M. L., Hoffmann, K. R., Katafuchi, T., Ohara, K., and Chan, H.-P., 1987, *Invest. Radiol.*, **22,** 328.

Fujita, H., Tsai, D.-Y., Itoh, T., Doi, K., Morishita, J., Ueda, K., and Ohtsuka, A., 1992, *IEEE Trans. Med. Imag.*, **11,** 34.

Gould, R. G., and Hale, J., 1974, *Am. J. Roentgenol.*, **122,** 109.

Grainger, R. G., and Allison, D. J., 1992, *Diagnostic Radiology: An Anglo-American Textbook of Imaging*, second edition (Edinburgh: Churchill Livingstone).

Harrison, R. M., 1985, *Phys. Med. Biol.*, **30,** 1335.

Hasegawa, B., 1991, *The Physics of Medical Imaging* (Madison: Medical Physics Publishing).

Heidsieck, R., 1989, Medical Imaging III: Image Formation, Proceedings of the SPIE, Vol. 1090 (Bellingham, Washington: SPIE), p. 222.

Hubbell, J. H., Veigle, W. J., Briggs, E. A., Brown, R. T., Cromer, D. T., and Howerton, R. J., 1975, *J. phys. chem. Ref. Data*, **4,** 471.

ICRU, 1992, *Photon, Electron, Proton and Neutron Interaction Data for Body Tissues*, ICRU Report No. 46 (Bethesda: International Commission on Radiation Units and Measurement), p. 122.

Johns, H. E., and Cunningham, J. R., 1983, *The Physics of Radiology*, fourth edition (Springfield, Virginia: CC Thomas).

Johns, P. C., and Yaffe, M. J., 1983, *Med. Phys.*, **10,** 40.

Kruger, D. G., Zink, F. E., Peppler, W. W., Ergun, D. L., and Mistretta, C. A., 1994, *Med. Phys.*, **21,** 175.

Kubota, H., Ozaki, Y., Matsumoto, M., and Kanamori, H., 1994, *Med. Biol. Engng Comput.*, **32,** 468.

Lo, J. Y., Floyd, C. E., Baker, J. A., and Ravin, C. E., 1994, *Med. Phys.*, **21,** 435.

Love, L. A., and Kruger, R. A., 1987, *Med. Phys.*, **14,** 178.

Love, L. A., Kruger, R. A., and Simons, M. A., 1986, Medicine XIV/PACS IV, Proceedings of the SPIE Vol. 626 (Bellingham, Washington: SPIE), p. 275.

Luhta, R., and Rowlands, J. A., 1990, *Med. Phys.*, **17,** 913.
Macovski, A., 1983, *Medical Imaging Systems* (Englewood Cliffs, New Jersey: Prentice-Hall).
Maher, K. P., and Greaves, A. W., 1992, *Austral. Phys. Engng Sci. Med.*, **15,** 95.
Maher, K. P., 1993, *Phys. Med. Biol.*, **38,** 1977.
Maher, K. P., and Malone, J. F., 1986, *Contemp. Phys.*, **27,** 533.
Maher, K. P., O'Connor, M. K., and Malone, J. F., 1987, *Phys. Med. Biol.*, **32,** 1273.
Marshall, N. W., Faulkner, K., Busch, H. P., Marsh, D. M., and Pfenning, H., 1994, *Br. J. Radiol.*, **67,** 353.
Molloi, S. Y., and Mistretta, C. A., 1988, *Med. Phys.*, **15,** 289.
Morin, R. L. (editor), 1988, *Monte Carlo Simulation in the Radiological Sciences* (Boca Raton, Florida: CRC Press).
Neitzel, U., Maack, I., and Günther-Kohfahl, S., 1994, *Med. Phys.*, **21,** 509.
Niklason, L. T., Sorenson, J. A., and Nelson, J. A., 1981, *Med. Phys.*, **8,** 677.
Noordveld, R. B., Schultze Kool, L. J., Kroon, H. M., Algra, P. R., Seeley, G. W., Lemmers, H. E., Vlasbloem, H., and Biebesheimer, V., 1989, Medical Imaging III: Image Formation, Proceedings of the SPIE, Vol. 1090 (Bellingham, Washington: SPIE), p. 78.
Plenkovich, D., 1989, *Acta Radiol. Suppl.*, **373,** 1.
Press, W. H., Flannery, B. P., Teukolsky, S. A., and Vettering, W. T., 1986, *Numerical Recipies: The Art of Scientific Computing* (London: Cambridge University Press), pp. 77–101.
Roeck, W. W., Martin, J. T., and Beach, R., 1992, *Med. Phys.*, **19,** 1201.
Rosenow, U. F., 1995, *Med. Phys.*, **22,** 1855.
Seibert, J. A., Nalcioglu, O., and Roeck, W. W., 1984, *Med. Phys.*, **11,** 172.
Seibert, J. A., Nalcioglu, O., and Roeck, W. W., 1985, *Med. Phys.*, **12,** 281.
Seibert, J. A., and Boone, J. M., 1988, *Med. Phys.*, **15,** 567.
Seibert, J. A., and Boone, J. M., 1989, Medical Imaging III: Image Processing, Proceedings of the SPIE, Vol. 1092 (Bellingham, Washington: SPIE), p. 356.
Shaw, C. G., Ergun, D. L., Myerowitz, P. D., VanLysel, M. S., Mistretta, C. A., Zarnstorff, W. C., and Crummy, A. B., 1982, *Radiology*, **142,** 209.
Shaw, C. G., and Plewes, D. B., 1985, *Radiology*, **157,** 247.
Shaw, C. C., 1992, Medical Imaging VI: Instrumentation, Proceedings of the SPIE, Vol. 1651 (Bellingham, Washington: SPIE), p. 164.
Sones, R. A., Lauro, K. L., and Cattell, C. L., 1990, *Radiology*, **175,** 553.
Sorenson, J. A., and Niklason, L. T., 1988, *Progress in Medical Imaging*, edited by V. L. Newhouse (New York: Springer), pp. 159–184.
Vosburgh, K. G., Swank, R. K., and Houston, J. M., 1977, *Adv. Electron. Electron Phys.*, **43,** 205.
Wagner, F. C., Macovski, A., and Nishimura, D. G., 1988a, *Med. Phys.*, **15,** 732.
Wagner, F. C., Macovski, A., and Nishimura, D. G., 1988b, *IEEE Trans. Med. Imag.*, **7,** 337.
Wagner, F. C., Macovski, A., and Nishimura, D. G. 1989, *Med. Phys.*, **16,** 747.
Webb, S. (editor), 1988, *The Physics of Medical Imaging* (Bristol: Institute of Physics).
White, K. S., Baxter, B., and Nelson, J. A., 1985, *Invest. Radiol.*, **20,** 854.

Associate Professor *Kieran Maher* is currently Head of the Department of Medical Radiations Science at the Royal Melbourne Institute of Technology in Australia. He has previously worked in the Department of Medical Physics and Bioengineering of the Federated Dublin Voluntary Hospitals and in the Physics Department of the Dublin Institute of Technology in Ireland. His research interests are in the physical aspects of medical imaging.

Professor *J. F. Malone* is Head of the Department of Medical Physics and Bioengineering at St James's Hospital and Federated Dublin Voluntary Hospitals, and is Director of Graduate Studies for the Faculty of Health Sciences, Trinity College Dublin. He graduated in physics from the National University of Ireland and previously worked for the West of Scotland Health Boards in Glasgow and at the Dublin Institute of Technology. He was recently elected to Fellowship of the Faculty of Radiologists of the Royal College of Surgeons in Ireland. His research interests include digital medical imaging, thyroid radiobiology and medical instrumentation.